Journal of Alloys and Compounds 863 (2021) 158500

Contents lists available at ScienceDirect

Journal of Alloys and Compounds

journal homepage: www.elsevier.com/locate/jalcom

# Composition and temperature dependent structural investigation of the perovskite-type sodium-ion solid electrolyte series $Na_{1/2-x}La_{1/2-x}Sr_{2x}ZrO_3$

Frederick Z.T. Yang[a], Vanessa K. Peterson[b,c], Siegbert Schmid[a,*]

[a] School of Chemistry, The University of Sydney, Sydney, NSW 2006, Australia
[b] Australian Centre for Neutron Scattering, Australian Nuclear Science and Technology Organisation, Lucas Heights, NSW 2234, Australia
[c] Institute for Superconducting and Electronic Materials, University of Wollongong, Squires Way, North Wollongong, NSW 2500, Australia

ARTICLE INFO

*Article history:*
Received 14 September 2020
Received in revised form 21 December 2020
Accepted 22 December 2020
Available online 7 January 2021

*Keywords:*
Solid-electrolyte
All-solid-state batteries
Na-ion battery
Perovskite-type
Phase transition

ABSTRACT

Owing to their vast chemical and structural flexibility, crystalline perovskite-type metal oxides ($ABO_3$) are amongst the most promising solid electrolytes for use in all-solid-state batteries for large scale energy storage applications. The perovskite-type sodium-ion solid electrolyte series $Na_{1/2-x}La_{1/2-x}Sr_{2x}ZrO_3$ have the highest reported ionic conductivities, and we re-examine their room temperature crystal structures using X-ray and high-resolution neutron powder diffraction. In contrast to a previous report, four members of the series, $x$ = 1/16, 1/8, 1/6, and 1/4, were found to adopt orthorhombic symmetry with the space group *Pbnm*. Variable temperature neutron diffraction data (room temperature to 1100 °C) were used to probe temperature-dependent structural changes for the member of the series with the highest reported ionic conductivity ($x$ = 1/6). A phase transition from orthorhombic *Pbnm* to tetragonal *I*4/*mcm* was identified at 800 °C.



## 1. Introduction

The development of high-performance sodium-ion batteries (SIBs) has recently attracted a lot of attention owing to the natural abundance of sodium resources [1,2]. This is particularly important for large scale energy storage, e.g. grid storage of sustainably sourced energy or electric vehicles [3,4]. Current rechargeable battery technologies' reliance on highly flammable organic based liquid electrolytes presents major safety concerns, in particular for electric vehicles [5–7]. To address these safety issues, the organic liquid electrolytes can be replaced by solid electrolytes to form all-solid-state batteries (ASSBs). Solid electrolytes offer many advantages over organic electrolytes. As no liquid is used in ASSBs, their packing may be simplified resulting in smaller size and increased energy density [8–11]. Importantly, the removal of highly flammable organic electrolytes allows for the safe operation of the battery over larger temperature ranges.

Perovskite-type oxides ($ABO_3$) are among the most intensively studied classes of solid electrolyte materials, owing to the flexibility and stability of this structure type. Inaguma et al. [12] synthesised and characterised $Li_{0.33}La_{0.55}TiO_3$ (LLT), where $Li^+$ and $La^{3+}$ occupy the *A*-site and $Ti^{4+}$ occupies the *B*-site. LLT showed high total ionic conductivity of $2 \times 10^{-5}$ S cm$^{-1}$ at room temperature, which was further increased by 50% through the introduction of $Sr^{2+}$ onto the *A*-site [13]. This was due to an expansion in cell dimensions driven by the larger ionic radius of $Sr^{2+}$ (1.44 Å [14]) compared to $Li^+$ and $La^{3+}$ (0.90 Å and 1.36 Å, respectively [14]), which improved the size of the bottleneck in the diffusion pathway for $Li^+$ ions. This system has been extensively investigated with high ionic conductivity reported upon various *A*- and *B*-site cation substitutions [15,16]. In addition, concerted octahedral rotations in these systems have been considered important for ionic conductivity [17,18].

Four members of the perovskite-type solid electrolyte system, $Na_{1/2-x}La_{1/2-x}Sr_{2x}ZrO_3$ (NLSZ), a sodium analogue to LLT, were recently synthesised and characterised by Zhao et al. [19]. The structures of four representatives were reported to adopt cubic symmetry with the space group $P2_13$. The assignment of this symmetry was based on a wrong structure for $SrZrO_3$, which has instead been shown many times to adopt *Pnma* symmetry at room temperature [20,21]. The cubic symmetry also appears highly unusual since both theoretical end members of the series, i.e. $SrZrO_3$ ($x$ = 0.5) and $Na_{1/2}La_{1/2}ZrO_3$ ($x$ = 0), adopt orthorhombic symmetry with *Pnma* space group [21,22]. There is no report in the literature of any substitutional perovskite solid solution where a member of the solid solution has a higher symmetry than both end members. Amongst the investigated compositions, the $x$ = 1/6 member of the

* Corresponding author.
*E-mail address:* siegbert.schmid@sydney.edu.au (S. Schmid).

https://doi.org/10.1016/j.jallcom.2020.158500
0925-8388/

system, $Na_{1/3}La_{1/3}Sr_{1/3}ZrO_3$, was reported to have the highest ionic conductivity of $1.025 \times 10^{-5}$ S cm$^{-1}$ at room temperature [19].

Given the very high sodium-ion conductivity of these phases and the scarcity and importance of such materials for future sodium-ion batteries, a careful re-investigation of the structures is warranted, given the unusual symmetry previously published [19]. This manuscript reports the synthesis and renewed structural characterisation of the NLSZ solid electrolyte series at room temperature using both X-ray and neutron powder diffraction data. In addition, structural changes for the member of the system with the highest reported ionic conductivity, i.e. $Na_{1/3}La_{1/3}Sr_{1/3}ZrO_3$ ($x$ = 1/6), are probed over a wide range of temperatures using neutron powder diffraction.

## 2. Experimental

Members of the $Na_{1/2-x}La_{1/2-x}Sr_{2x}O_3$ system ($x$ = 1/16, 1/8, 1/6, 1/4) were synthesised via solid-state reaction. Bulk amounts of starting reagents $Na_2CO_3$ (Merk, 99.9%), $SrCO_3$ (Aldrich 99.9%), and $ZrO_2$ (Aldrich 99%) were dried at 200 °C with the exception of $La_2O_3$ (Aithaca 99.98%), which was heated at 1000 °C for 15 h to remove any traces of moisture or carbon dioxide. Stoichiometric amounts of reagents were ground using a mortar and pestle, adding 10 wt% excess of $Na_2CO_3$ to compensate for possible sodium loss at high temperatures. The polycrystalline mixtures were annealed at 900 °C for 10 h, reground, and then pressed into ~5 cm rods using a hydrostatic press before being annealed at 1300 °C for a further 10 h.

All samples were characterised using X-ray powder diffraction (XRPD) at Sydney Analytical. Samples were loaded into glass capillaries (0.5 mm diameter) and mounted on a spinning capillary stage. Data were collected on a STOE STADI P diffractometer using Mo-$K_{\alpha1}$ radiation ($\lambda$ = 0.70932 Å) in Debye-Scherrer geometry over the range 5° < 2θ < 55° with triple MYTHEN 1K detectors at room temperature (20-minute scans).

All samples were further analysed using neutron powder diffraction (NPD) at the Australian Centre for Neutron Scattering (ACNS) of the Australian Nuclear Science and Technology Organisation (ANSTO). NPD was carried out using the high-resolution neutron powder diffractometer Echidna [23] with the $La^{11}B_6$ (NIST SRM 660b) standard reference material. All samples were sealed in 9 mm vanadium cans and data collected using a neutron wavelength of 2.4394(5) Å from 5° < 2θ < 160° 2θ over a period of 5 h at room temperature.

Variable temperature NPD data for $Na_{1/3}La_{1/3}Sr_{1/3}ZrO_3$ were obtained using the high intensity neutron powder diffractometer Wombat [24] from room temperature to 1100 °C. The sample was sealed in a 9 mm vanadium can and inserted into a 1600 °C ILL-type high-vacuum furnace. Data were collected using a neutron wavelength of 2.4132(4) Å with the 331 reflection of a vertically focusing Ge monochromator at a heating rate of 5 °C per minute from room temperature to 400 °C and 1 °C per minute from 400 to 1100 °C with 1 min scans per degree step during heating and cooling.

Structural characterisation was performed with both XRPD and NPD data using the Rietveld method implemented in software package TOPAS Academic (v5) [25]. The background was fitted using a Chebyshev polynomial with eight terms.

## 3. Results and discussion

Members of the $Na_{1/2-x}La_{1/2-x}Sr_{2x}O_3$ system with $x$ = 1/16, 1/8, 1/6, and 1/4, were previously reported with unusual cubic symmetry and high ionic conductivity, which reached $1.025 \times 10^{-5}$ S cm$^{-1}$ at room temperature for the x = 1/6 phase [19]. Owing to the enormous interest in such Na-ion conductors and the inherent connection between ionic conductivity and symmetry, the structures of these materials were re-investigated. The phases were synthesised via conventional solid-state techniques and their structures characterised using XRPD and NPD data.

### 3.1. X-ray powder diffraction

XRPD patterns of the samples collected at room temperature showed peak splitting as well as several very weak reflections, as can be seen in Fig. 1. It is evident that these weak reflections do not match the previous cubic model well (red peak markers) [19]. The combination of weak reflections and peak splitting, however, suggests the series adopts a lower symmetry than previously reported. Indeed, it was possible to index the XRPD data for the four members of the series investigated here to an orthorhombic symmetry described by the same space group, *Pbnm* (note that *Pbnm* is an alternate setting for *Pnma*). This is therefore in agreement with the symmetry of both theoretical end members, $SrZrO_3$ and $Na_{1/2}La_{1/2}ZrO_3$, as mentioned above [21,22]. Hence, the presence of weak reflections between ~15 and ~24° 2θ is characteristic of the orthorhombic symmetry of a perovskite-type structure, rather than impurity phases previously reported (Figs. 1 and 2).

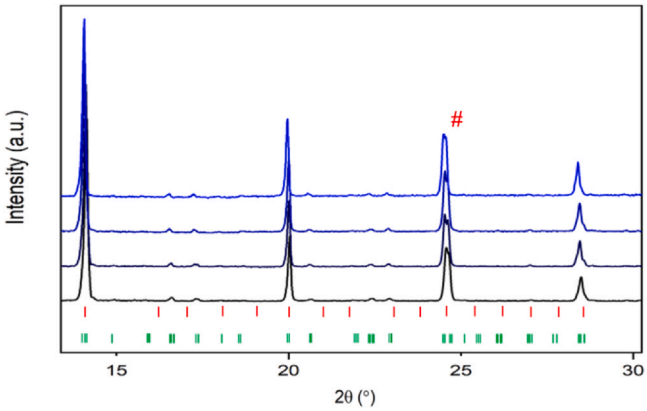


**Fig. 1.** Diagnostic section of the XRPD patterns of the $Na_{1/2-x}La_{1/2-x}Sr_{2x}ZrO_3$ series showing signs of splitting (marked by #) and weak reflections (from x = 1/4 top to 1/16 bottom). The red peak markers indicate Bragg reflections expected for the cubic $P2_13$ perovskite model of Zhao et al. [19] and the green peak markers indicate the Bragg reflections consistent with the orthorhombic space group *Pbnm*. Data are offset in y for clarity. (For interpretation of the references to colour in this figure legend, the reader is referred to the web version of this article.)

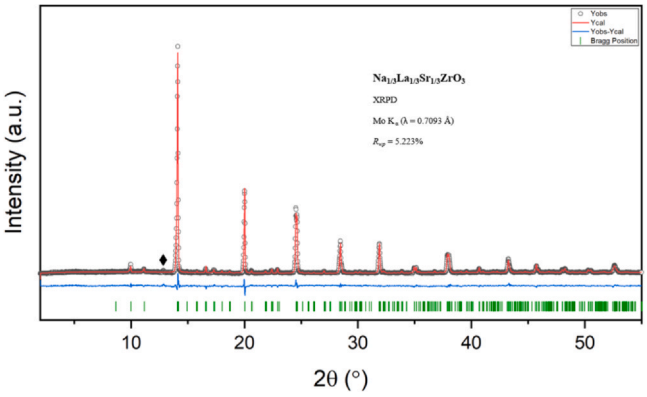


**Fig. 2.** Rietveld refinement profile using XPRD data of $Na_{1/3}La_{1/3}Sr_{1/3}ZrO_3$. The observed pattern is marked by (o), the calculated pattern is shown by the red line and the difference between calculated and observed patterns is shown in blue. Bragg positions for the orthorhombic *Pbnm* symmetry are indicated by the green tick marks. $R_{wp}$ is the weighted profile R-factor. The black diamond marks an impurity reflection assigned to $ZrO_2$. (For interpretation of the references to colour in this figure legend, the reader is referred to the web version of this article.)

**Table 1**
Unit cell parameters, in the pseudo-cubic setting, obtained from Rietveld refinement against XRPD data for $Na_{1/2-x}La_{1/2-x}Sr_{2x}ZrO_3$, and the cubic unit cell parameters reported by Zhao et al. [19].

| x | a (Å) | b (Å) | c (Å) | Volume (Å$^3$) | Zhao et al. (Å) |
|---|---|---|---|---|---|
| 1/16 | 4.08944(4) | 4.07775(4) | 4.06179(4) | 67.73325(2) | 4.07056 |
| 1/8 | 4.09045(4) | 4.07931(4) | 4.06115(4) | 67.76522(2) | 4.07675 |
| 1/6 | 4.08977(4) | 4.08188(4) | 4.06491(4) | 67.85941(2) | 4.08145 |
| 1/4 | 4.09367(4) | 4.08587(4) | 4.07075(4) | 68.08819(2) | 4.08841 |

In particular, the weak reflection at ~16.5° 2θ corresponds to the reflection at ~36° 2θ in Zhao et al.'s Fig. 2a. There it is identified as a $La_2Zr_2O_7$ reflection. That reflection, however, would appear at ~33° 2θ, should be lower in intensity than the reflection at ~29° 2θ and these two reflections should not change relative intensity across the four patterns. Na, La, and Sr share the *A*-site in the centre of the unit cell, while Zr occupies the *B*-site on the corners of the unit cell. The orthorhombic symmetry has two crystallographically independent oxygen sites that form the octahedron around the *B*-site cation. The Zr–O distances are ~2.09 Å to O1 (x2) and ~2.09 Å to O2 (x4), confirming that the octahedra are almost regular (see Table S1).

It is evident that as $Na^+$ and $La^{3+}$ ions were substituted by $Sr^{2+}$, the diffraction peaks shifted towards lower 2θ angles (Fig. 1). This shift indicates an expansion of the unit cell as $Sr^{2+}$ is substituted for $Na^+$ and $La^{3+}$ on the *A*-site. This is expected given the relative differences in effective ionic radii ($Na^+$ = 1.39 Å, $La^{3+}$ = 1.36 Å, $Sr^{2+}$ = 1.44 Å, all three in 12-fold coordination [14]), and is consistent with trends reported for perovskite-type Li-ion solid electrolytes [13]. The unit cell parameters of the orthorhombic *Pbnm* perovskite can be described in terms of the ideal cubic perovskite given by $a \sim \sqrt{2}\,a_p$, $b \sim \sqrt{2}\,a_p$, and $c \sim 2a_p$, where $a_p$ is the length of an ideal cubic perovskite unit cell. Unit cell parameters obtained from Rietveld refinement for each member of the series were converted to the pseudo-cubic values for ease of comparison with those reported by Zhao et al. [19] (Table 1). The unit cell volume increases with increasing $Sr^{2+}$ substitution

### 3.2. Neutron powder diffraction

The weak superstructure reflections observed in the XRPD data are due to tilting of octahedra, which cause the oxygen atoms to move from their high-symmetry positions. For a detailed analysis of the octahedral tilting within the perovskite structure, NPD data were used owing to the relatively larger scattering from oxygen compared to the heavier metal atoms. High-resolution NPD data collected at room temperature on Echidna for all members of the series showed the presence of *R*-point and *M*-point superlattice reflections, with *h, k, l* = odd, odd, even, and odd, even, even, indices in the pseudo-cubic double-perovskite setting, respectively, indicative of the presence of both in- and out-of-phase tilting of the $BO_6$ octahedra. The combination of both tilts within the structure resulted in the appearance of additional *X*-point reflections (Fig. 3). Using Rietveld refinement against the NPD patterns for all four members of the series confirmed the orthorhombic symmetry described by the space group *Pbnm*, consistent with XPRD data analysis (Table 2). All members of the series were found to have out-of-phase tilting of the $BO_6$ octahedra about the $[100]_p$ and $[010]_p$ axes with an in-phase tilt along the $[001]_p$ axis of the pseudo-cubic perovskite (Fig. 4), denoted in Glazer's notation as $a^- a^- c^+$ [26]. The Goldschmidt tolerance factor was calculated to be 0.937, consistent with the tilts observed in this perovskite system [27]. Due to the mixed nature of the *A*-site, the mean ionic radius of $Na^+$, $La^{3+}$, and $Sr^{2+}$ was used to calculate the tolerance factor.

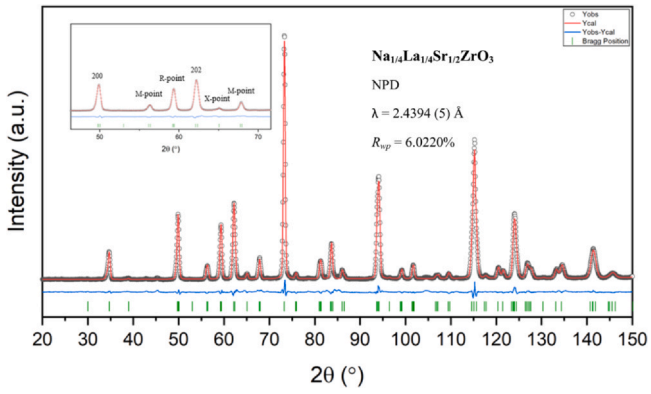


**Fig. 3.** Rietveld refinement profile using NPD data of $Na_{1/4}La_{1/4}Sr_{1/2}ZrO_3$. The observed pattern is marked by (o), the calculated pattern shown in red and the difference between calculated and observed patterns is shown in blue. Bragg positions for the orthorhombic *Pbnm* symmetry are indicated by the green tick marks. The inset from 50° < 2θ < 70° highlights the superlattice reflections that are characteristic of octahedral tilting within a perovskite-type structure. $R_{wp}$ is the weighted profile R-factor. (For interpretation of the references to colour in this figure legend, the reader is referred to the web version of this article.)

**Table 2**
Space group and refined atomic parameters for $Na_{1/2-x}La_{1/2-x}Sr_{2x}ZrO_3$ using Echidna data collected at room temperature. Figures of merit are the Bragg R-factor $R_{Bragg}$ and the reduced chi-squared $\chi^2$.

| Sample (x) | 1/16 | 1/8 | 1/6 | 1/4 |
|---|---|---|---|---|
| Space Group | *Pbnm* | *Pbnm* | *Pbnm* | *Pbnm* |
| Na/La/$Sr_x$ | -0.00449 (3) | -0.00396 (3) | -0.00408 (3) | -0.00680 (4) |
| Na/La/$Sr_y$ | 0.48161 (3) | 0.47745 (4) | 0.47429 (4) | 0.47494 (4) |
| Na/La/$Sr_z$ | 0.25 | 0.25 | 0.25 | 0.25 |
| $B_{iso}$ | 1.12853(1) | 1.27822(1) | 1.03462(1) | 0.75763(2) |
| $Zr_x$ | 0 | 0 | 0 | 0 |
| $Zr_y$ | 0 | 0 | 0 | 0 |
| $Zr_z$ | 0 | 0 | 0 | 0 |
| $B_{iso}$ | 0.35313(2) | 0.51755(1) | 0.23168(2) | 0.29730(2) |
| $O1_x$ | 0.07872(3) | 0.07746(3) | 0.07790(3) | 0.07317(4) |
| $O1_y$ | 0.01513(3) | 0.01534(4) | 0.01734(4) | 0.01598(4) |
| $O1_z$ | 0.25 | 0.25 | 0.25 | 0.25 |
| $B_{iso}$ | 0.27249(1) | 0.75695(1) | 0.67026(1) | 0.38328(2) |
| $O2_x$ | 0.21113(4) | 0.21065(4) | 0.20997(4) | 0.21176(4) |
| $O2_y$ | 0.28895(4) | 0.28882(4) | 0.29023(5) | 0.28700(4) |
| $O2_z$ | -0.03964(4) | -0.03867(4) | -0.03779(3) | -0.03690(4) |
| $B_{iso}$ | 0.92204(1) | 0.99471(1) | 0.85226(2) | 0.77680(2) |
| $R_{Bragg}$ (%) | 5.58 | 4.27 | 4.08 | 2.02 |
| $\chi^2$ | 6.89 | 7.05 | 7.20 | 3.21 |

#### 3.2.1. Variable temperature structural characterisation

Variable temperature NPD data were collected for the member of the $Na_{1/2-x}La_{1/2-x}Sr_{2x}ZrO_3$ series with the highest ionic-conductivity, $x = 1/6$ ($Na_{1/3}La_{1/3}Sr_{1/3}ZrO_3$) as previously reported [19], using the Wombat diffractometer from ambient temperature to 1100 °C. Reflections in the diffraction patterns were found to shift towards lower 2θ angles on heating, indicating expansion of the unit cell with increasing temperature (Fig. 5).

The integrated intensities of the *M*- and *R*-point super lattice reflections at ~56° and ~59°, respectively, were extracted from sequential single-peak analysis using TOPAS Academic (v5). The peak shape was modelled using a pseudo-Voigt function. For the orthorhombic *Pbnm* phase, the integrated intensity of the *M*-point with *hkl* indices 120 and 210, denoted by $I(120+210)_{Pbnm}$, continuously decreased with increasing temperature. The intensity of $I(120+210)_{Pbnm}$ represents the amplitude of the in-phase tilting of successive layers about the $[001]_p$ axis of the pseudo-cubic perovskite. This corresponds to the $M_3$ point of the cubic Brillouin zone [28]. This peak was undetectable from 800 °C (Fig. 6a), consistent with an orthorhombic *Pbnm* to tetragonal *I*4/*mcm* phase transition. Integrated intensities of the *R*-point with *hkl* indices

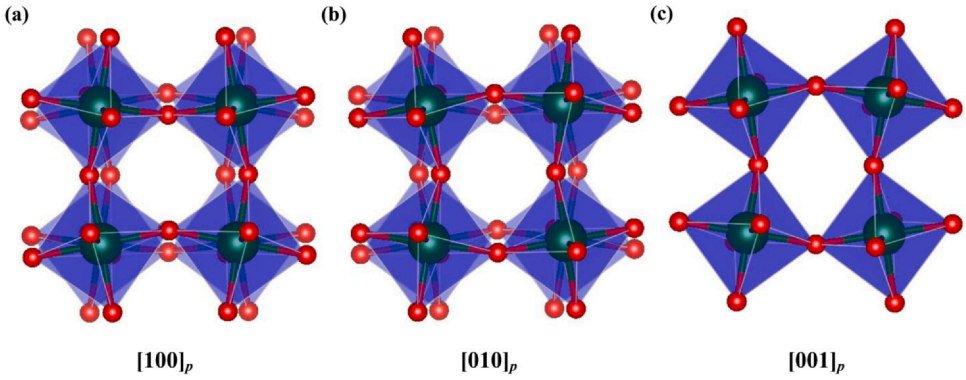


**Fig. 4.** Representation of octahedral tilting within the orthorhombic Pbnm space group. $BO_6$ octahedra are blue, B-site metal position green and O atoms are red. (a) and (b) represent out-of-phase tilting along the $[100]_p$ and $[010]_p$ axes and (c) represents in-phase tilting along the $[001]_p$ axis with respect to the pseudo-cubic perovskite. (For interpretation of the references to colour in this figure legend, the reader is referred to the web version of this article.)

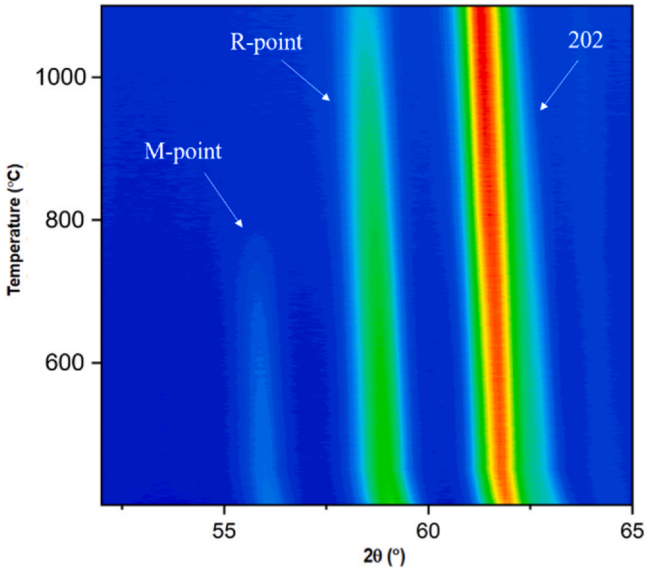


**Fig. 5.** Variable temperature NPD data for $Na_{1/3}La_{1/3}Sr_{1/3}ZrO_3$ from Wombat between room temperature and 1100 °C using λ = 2.4132(4) Å neutrons. Intensity ranges from lowest (blue) to highest (red) and highlights the decrease in intensity of the *M*- and *R*-point superlattice reflection with increasing temperature. (For interpretation of the references to colour in this figure legend, the reader is referred to the web version of this article.)

121, 211, and 103 denoted by $I(121 + 211 + 103)_{Pbnm}$ also decreased with increasing temperature (Fig. 6b). The intensity $I(121 + 211 + 103)_{Pbnm}$ is related to the amplitude of the out-of-phase tilting of the $BO_6$ octahedra about the $[100]_p$ and $[010]_p$ direction of the pseudo-cubic perovskite [20,29,30]. This corresponds to the $R_{25}$ point of the cubic Brillouin zone, and can also be described as a single out-of-phase tilt about the $[110]_p$ axis of the octahedron [28]. For the transition at 800 °C, according to the group theoretical analysis by Howard and Stokes [28], three space groups are possible with out-of-phase tilting only, *R*3*c* ($a^- a^- a^-$), *Imma* ($a^0 b^- b^-$), or *I*4/*mcm* ($a^0 a^0 c^-$). The x = 0.5 theoretical end member $SrZrO_3$ was found by Howard et al. [20] to have phase transitions from room temperature to 1230 °C of *Pnma* → *Imma* → *I*4/*mcm* → *Pm*3*m*. The continuity in the decrease of the *R*-point intensity suggests the structure might undergo a second order continuous transition to *Imma,* i.e. following the high temperature phase transitions of $SrZrO_3$. As both the *Imma* and *I*4/*mcm* space groups have the same characteristic *R*-point reflections, the difference between the space groups was reported to be the splitting of the $002_p$ diffraction peak for $SrZrO_3$ [20]. However, no splitting was observed for the $002_p$ diffraction peak in $Na_{1/3}La_{1/3}Sr_{1/3}ZrO_3$ around 800 °C. Hence, the *R*-point peak intensities $I(121 + 211 + 103)_{Pbnm}$ are now represented as $I(211)_{I4/mcm}$ as the structure undergoes a first order transition from orthorhombic *Pbnm* to tetragonal *I*4/*mcm* (Fig. 6b). No additional transitions were found between 800 and 1100 °C, as reflected by the continuing presence of the *R*-point reflection. This is consistent with the previously reported high temperature *Pbnm* – *I*4/*mcm* transitions in perovskite structures [20,29,31].

Sequential Rietveld refinements were performed against the variable temperature Wombat data from room temperature to 800 °C in the orthorhombic space group *Pbnm*. Against data from 800 to 1100 °C, structural models were refined in the space group *I*4/*mcm* ($a^0 a^0 c^-$) with a single out-of-phase tilt along the $[001]_p$ axis (Fig. 7).

In the high-temperature *I*4/*mcm* phase Na, La, and Sr occupy the *A*-site position in the centre of the unit cell, while Zr occupies the corners (Table 3). There are still two crystallographically independent oxygen sites in the structure, however, O1 now has no refinable positional parameters while O2 has only 1 instead 2. The Zr–O distances are ~2.06 Å to O1 (x2) and ~2.09 Å to O2 (x4), confirming that the octahedra are slightly squashed along the c-direction (see Table S2).

## 4. Conclusion

The perovskite-type sodium-ion solid electrolyte series $Na_{1/2-x}La_{1/2-x}Sr_{2x}ZrO_3$ (x = 1/16, 1/8, 1/6, 1/4) was synthesised using solid-state techniques and the structures successfully determined. Using X-ray and neutron powder diffraction data collected at room temperature, all four investigated members of the series were found to have orthorhombic symmetry described by the space group *Pbnm* ($a^- a^- c^+$). This is in contrast to the previous conclusion by Zhao et al. [19] that this perovskite system adopts cubic $P2_13$ space-group symmetry. Our result is consistent with the structures for the theoretical endmembers x = 0 and x = 0.5, i.e. $Na_{1/2}La_{1/2}ZrO_3$ and $SrZrO_3$ [21,22], respectively, also adopting *Pbnm* space-group symmetry, and with group theoretical considerations [28]. The progressive replacement of $Na^+$ and $La^{3+}$ with the larger $Sr^{2+}$ cation on the *A*-site resulted in an increase of the unit cell parameters.

In addition, a structural phase transition was found for the *x* = 1/6 member of the series ($Na_{1/3}La_{1/3}Sr_{1/3}ZrO_3$) using variable temperature neutron powder diffraction data collected from room temperature to 1100 °C. Through the analysis of integrated intensities, the structure of $Na_{1/3}La_{1/3}Sr_{1/3}ZrO_3$ was found to undergo a phase transition from orthorhombic *Pbnm* ($a^- a^- c^+$) to tetragonal *I*4/*mcm* ($a^0 a^0 c^-$) at 800 °C.

The accurate structure determination for this solid-electrolyte system will allow for a better understanding of the structure — property relationship and targeted improvements through chemical and structural modifications.

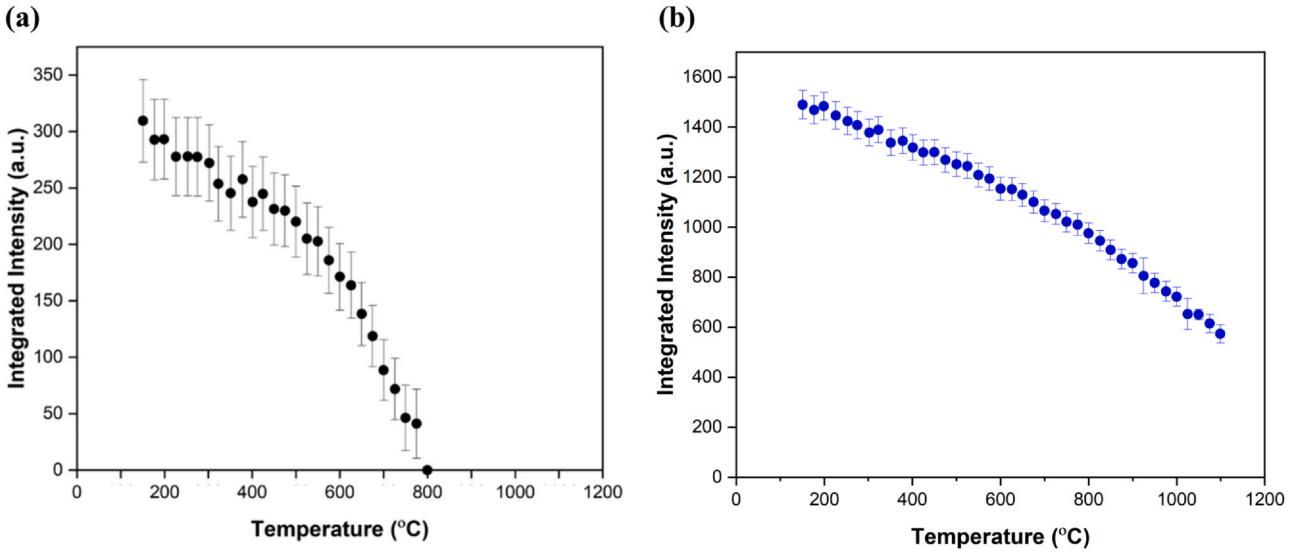


**Fig. 6.** Temperature dependence of integrated intensities of $Na_{1/3}La_{1/3}Sr_{1/3}ZrO_3$ reflections obtained from single peak fitting. (a) Orthorhombic *M*-point 120 and 210 reflections, $I(120+210)_{Pbnm}$. (b) Orthorhombic *R*-point 121, 103, and 210 reflections, $I(121+103+211)_{Pbnm}$ as well as the tetragonal 211 reflection, $I(211)_{I4/mcm}$.

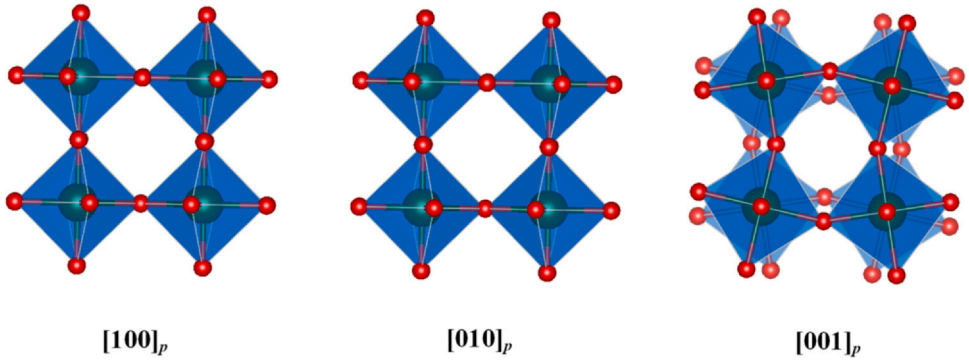


**Fig. 7.** Representation of the change in direction for the out-of-phase tilt from $[100]_p$ and $[010]_p$ axes to the $[001]_p$ axis for a first order discontinuous transition from Pbnm to *I*4/*mcm* space group symmetry, representing the tilt system $a^0\ a^0\ c^-$. $BO_6$ octahedra are blue and O atoms are red. (For interpretation of the references to colour in this figure legend, the reader is referred to the web version of this article.)

**Table 3**
Space group and refined atomic positions for $Na_{1/3}La_{1/3}Sr_{1/3}O_3$ from Wombat data collected at 850 °C.

| Space group | *I*4/*mcm* |
|---|---|
| $Na/La/Sr_x$ | 0 |
| $Na/La/Sr_y$ | 0.5 |
| $Na/La/Sr_z$ | 0.25 |
| $B_{iso}$ [Å$^2$] | 1.69081(1) |
| $Zr_x$ | 0 |
| $Zr_y$ | 0 |
| $Zr_z$ | 0 |
| $B_{iso}$ [Å$^2$] | 0.91370(1) |
| $O1_x$ | 0 |
| $O1_y$ | 0 |
| $O1_z$ | 0.25 |
| $B_{iso}$ [Å$^2$] | 3.46111(1) |
| $O2_x$ | 0.29799 (3) |
| $O2_y$ | 0.79799 |
| $O2_z$ | 0 |
| $B_{iso}$ [Å$^2$] | 3.77866 (1) |
| $R_{Bragg}$ [%] | 5.96 |
| $\chi^2$ | 4.02 |

## CRediT authorship contribution statement

The manuscript was written based on contributions from all authors.

## Declaration of Competing Interest

The authors declare that they have no known competing financial interests or personal relationships that could have appeared to influence the work reported in this paper.

## Acknowledgments

We acknowledge and pay respect to the Gadigal people of the Eora Nation, the traditional owners of the land on which this research was conducted. We thank Sydney Analytical, a core research facility at the University of Sydney, for help with characterisation of samples and financial support. Neutron powder diffraction data were collected at the Australian Centre for Neutron Scattering

(ACNS) of the Australian Nuclear Science and Technology Organisation and we are thankful for the provision of beam time.

## Appendix A. Supporting information

Supplementary data associated with this article can be found in the online version at doi:10.1016/j.jallcom.2020.158500.

## References

[1] C.P. Grey, J.M. Tarascon, Sustainability and in situ monitoring in battery development, Nat. Mater. 16 (2017) 45–56.
[2] D. Larcher, J.M. Tarascon, Towards greener and more sustainable batteries for electrical energy storage, Nat. Chem. 7 (2015) 19–29.
[3] B. Dunn, H. Kamath, J.M. Tarascon, Electrical energy storage for the grid: a battery of choices, Science 334 (2011) 928–935.
[4] Z.G. Yang, J.L. Zhang, M.C.W. Kintner-Meyer, X.C. Lu, D.W. Choi, J.P. Lemmon, J. Liu, Electrochemical energy storage for green grid, Chem. Rev. 111 (2011) 3577–3613.
[5] J.B. Goodenough, Y. Kim, Challenges for rechargeable Li batteries, Chem. Mater. 22 (2010) 587–603.
[6] M. Armand, J.M. Tarascon, Building better batteries, Nature 451 (2008) 652–657.
[7] W. Li, J.R. Dahn, D.S. Wainwright, Rechargeable lithium batteries with aqueous electrolytes, Science 264 (1994) 1115–1118.
[8] J.B. Goodenough, P. Singh, Review—solid electrolytes in rechargeable electrochemical cells, J. Electrochem. Soc. 162 (2015) A2387–A2392.
[9] M. Guin, F. Tietz, O. Guillon, New promising NASICON material as solid electrolyte for sodium-ion batteries: correlation between composition, crystal structure and ionic conductivity of $Na_{3+x}Sc_2Si_xP_{3-x}O_{12}$, Solid State Ion. 293 (2016) 18–26.
[10] V. Thangadurai, D. Pinzaru, S. Narayanan, A.K. Baral, Fast solid-state Li ion conducting garnet-type structure metal oxides for energy storage, J. Phys. Chem. Lett. 6 (2015) 347.
[11] F. Zheng, M. Kotobuki, S.F. Song, M.O. Lai, L. Lu, Review on solid electrolytes for all-solid-state lithium-ion batteries, J. Power Sources 389 (2018) 198–213.
[12] Y. Inaguma, L.Q. Chen, M. Itoh, T. Nakamura, T. Uchida, H. Ikuta, M. Wakihara, High ionic conductivity in lithium lanthanum titanate, Solid State Commun. 86 (1993) 689–693.
[13] Y. Inaguma, L.Q. Chen, M. Itoh, T. Nakamura, Candidate compounds with perovskite structure for high lithium ionic conductivity, Solid State Ion. 70–71 (1994) 196–202.
[14] R.D. Shannon, Revised effective ionic radii and systematic studies of interatomic distances in halides and chalcogenides, Acta. Crystallogr. A32 (1976) 751–767.
[15] Y.D. Sun, P.Y. Guan, Y.J. Liu, H.L. Xu, S.A. Li, D.W. Chu, Recent progress in lithium lanthanum titanate electrolyte towards all solid-state lithium ion secondary battery, Crit. Rev. Solid State Mater. Sci. 44 (2019) 265–282.
[16] W.R. Brant, S. Schmid, A. Kuhn, J. Hester, M. Avdeev, M. Sale, Q. Gu, Rapid lithium insertion and location of mobile lithium in the defect perovskite $Li_{0.18}Sr_{0.66}Ti_{0.5}Nb_{0.5}O_3$, ChemPhysChem 13 (2012) 2293–2296.
[17] J. Sanz, J.A. Alonso, A. Varez, M.T. Fernandez-Diaz, Octahedral tilting and ordering of vacancies in the fast ion conductor $Li_{0.12}La_{0.63}TiO_3$ perovskite: a neutron diffraction study, J. Chem. Soc. Dalton Trans. (2002) 1406–1408.
[18] W.R. Brant, M. Roberts, T. Gustafsson, J.J. Biendicho, S. Hull, H. Ehrenberg, K. Edström, S. Schmid, A large format in operando wound cell for analysing the structural dynamics of lithium insertion materials, J. Power Sources 336 (2016) 279–285.
[19] Y.Z. Zhao, Z.Y. Liu, J.X. Xu, T.F. Zhang, F. Zhang, X.G. Zhang, Synthesis and characterization of a new perovskite-type solid-state electrolyte of $Na_{1/3}La_{1/3}Sr_{1/3}ZrO_3$ for all-solid-state sodium-ion batteries, J. Alloy. Compd. 783 (2019) 219–225.
[20] C.J. Howard, K.S. Knight, B.J. Kennedy, E.H. Kisi, The structural phase transitions in strontium zirconate revisited, J. Phys. Condens. Matter 12 (2000) L677–L683.
[21] B.J. Kennedy, C.J. Howard, B.C. Chakoumakos, High-temperature phase transitions in $SrZrO_3$, Phys. Rev. B 59 (1999) 4023–4027.
[22] M.C. Knapp, P.M. Woodward, J. Solid, A-site cation ordering in $AA'BB'O_6$ perovskites, J. Solid State Chem. 179 (2006) 1076–1085.
[23] K.D. Liss, B. Hunter, M. Hagen, T. Noakes, S. Kennedy, Echidna—the new high-resolution powder diffractometer being built at OPAL, Phys. B Condens. Matter 385–386 (2006) 1010–1012.
[24] A.J. Studer, M.E. Hagen, T.J. Noakes, Wombat: the high-intensity powder diffractometer at the OPAL reactor, Physica B 385–86 (2006) 1013–1015.
[25] A.A. Coelho, J.S.O. Evans, I.R. Evans, A. Kern, S. Parsons, The TOPASsymbolic computation system, Powder Diffr. 26 (2011) S22–S25.
[26] A.M. Glazer, The classification of tilted octahedra in perovskites, Acta. Crystallogr. B28 (1972) 3384–3392.
[27] V.M. Goldschmidt, Die Gesetze der Krystallochemie, Naturwissenschaften 14 (1926) 477–485.
[28] C.J. Howard, H.T. Stokes, Group-theoretical analysis of octahedral tilting in perovskites, Acta. Crystallogr. B54 (1998) 782–789.
[29] M. Yashima, R. Ali, Structural phase transition and octahedral tilting in the calcium titanate perovskite $CaTiO_3$, Solid State Ion. 180 (2009) 120–126.
[30] Y.S. Zhao, D.J. Weidner, J.B. Parise, D.E. Cox, Thermal expansion and structural distortion of perovskite — data for $NaMgF_3$ perovskite. Part I, Phys. Earth Planet. Inter. 76 (1993) 1–16.
[31] F. Guyot, P. Richet, P. Courtial, P. Gillet, High-temperature heat capacity and phase transitions of $CaTiO_3$ perovskite, Phys. Chem. Miner. 20 (1993) 141–146.